RSC Advances

PAPER

View Article Online
View Journal | View Issue

Cite this: *RSC Adv.*, 2017, **7**, 45662

Internal short circuit mitigation of high-voltage lithium-ion batteries with functional current collectors

Meng Wang,[a] Yang Shi,[b] Daniel J. Noelle,[b] Anh V. Le,[a] Hyojung Yoon,[c] Hyeseung Chung,[c] Minghao Zhang,[c] Ying Shirley Meng[c] and Yu Qiao*[ab]

Received 27th July 2017
Accepted 19th September 2017

DOI: 10.1039/c7ra08277k

rsc.li/rsc-advances

The safety of lithium-ion battery (LIB) becomes increasingly critical as the specific energy and cell capacity rapidly increase. Based on the modified current collector technique recently developed for nickel–cobalt–manganese active materials, here we investigate high-energy LIBs based on functional current collectors (FCC). Two high-voltage active materials were tested in our experiments: lithium-rich layered oxide (LRLO) and lithium nickel manganese oxide (LNMO). At the same time as a fully charged LIB cell is damaged, FCC isolates the internal short circuit (ISC) from the undamaged area; hence, the ISC-induced heat generation is drastically reduced to a negligible level. The electrochemical performance of FCC-based cells is nearly identical to that of reference cells.

1. Introduction

The lithium-ion battery (LIB) offers a promising solution for large-scale energy storage for electric vehicles (EV), data centers, smart grids, among others.[1–3] With the growing demand for high specific energy, high-voltage high-energy battery chemistry is under extensive research. It is envisioned that in 10–20 years, the specific energy of commercial LIB cells may exceed 300–400 W h kg^{-1},[4] nearly 1/4 of the specific energy of trinitrotoluene (TNT).[5] While the cost-performance balance has been much improved, the high energy leads to serious fire and explosion concerns. In conventional battery cell design, robustness was sometimes regarded as a secondary issue; yet the recent fire accidents in Boeing 787,[6,7] Tesla model S,[8,9] and Samsung Note 7 cell phones[10,11] suggest that LIB cell safety can be the "bottleneck" of the power system.

During normal operation, occasional mild electrical or thermal abuse on LIB cell can be handled by external safety features, such as battery management system,[12] battery thermal manage system,[13] and circuit breaking devices.[14] Upon intense mechanical abuse, *e.g.* EV collision, however, the external safety components could fail. Crash or metal penetration of LIB cell may form internal short circuits (ISC),[15] rapidly heating up the cell to the decomposition temperature of active materials.[16] The exothermal reactions further accelerate as temperature rises, causing thermal runaway.[17] The consequence of thermal runaway is often severe: the organic components (*e.g.* ethylene carbonate and ethyl methyl carbonate) in electrolyte are highly flammable, and can be easily ignited by sparking from ISC;[18] decomposition of active materials generate oxygen, which promotes combustion and even explosion.[19]

To avoid thermal runaway, it is essential to limit the heat generation rate of ISC. Conventional thermal-runaway mitigation approaches are often thermally triggered, including shutdown separators,[20,21] positive temperature coefficient additives and coatings,[22] and thermally sensitive binders.[23,24] Their time of reaction is usually slow compared to the aggressive temperature rise of ISC.[25] They take effect after cell temperature exceeds a certain threshold value, typically above 120–150 °C, dangerously close to the thermal runaway point. Faster and more efficient cell safety techniques must be developed for high-energy large-capacity LIB systems under threat of intense impact or penetration.

One way to significantly shorten the time of reaction is to use mechanically triggered mechanisms. Compared with the active material layer,[26–29] in an electrode, the current collector is much more critical for ISC formation,[30] since it accounts for more than 90% of the electrode strength and electrical conductivity. If the current collector is not made of flat metal sheets, but contain appropriate surface grooves, the fracture pattern can be favorably controlled as the cell is mechanically abused, leading to complete separation of the ISC site and the rest of electrode. Such a process occurs at the same time when the cell damage happens, before temperature increase begins.

Our testing data have shown that if the active material is nickel–cobalt–manganese (NCM) 523, modified current correct can successfully reduce the peak temperature of abused LIB

[a]*Department of Structural Engineering, University of California – San Diego, La Jolla, CA 92093-0085, USA. E-mail: yqiao@ucsd.edu*

[b]*Program of Materials Science and Engineering, University of California – San Diego, La Jolla, CA 92093, USA*

[c]*Department of Nanoengineering, University of California – San Diego, La Jolla, CA 92093, USA*

cells by ~90%.[31] While this finding is encouraging, there are still a couple of issues: first, previously the modification of current collector was conducted by etching, which was time-consuming and incompatible with the current LIB manufacturing methods. Second, there have not been any data about whether the modified current collector technique can be applied to higher-voltage higher-energy battery chemistry.

In the current research, we investigated debossing of current collectors. The modified current collectors were tested with two high-voltage active materials in impact and cycling experiments: lithium-rich layered oxide (LRLO) and lithium nickel manganese oxide (LNMO). LRLO is considered either as a solid solution or as a nanocomposite of layered Li_2MnO_3 and $Li(TM)O_2$ (TM = Ni, Co, Mn) with excess lithium ions in the transition metal layer. Upon lithium extraction, both nickel and cobalt are oxidized to Ni^{4+} and Co^{4+} up to 4.4 V. Lithium will continue to be extracted, with transition metal ions in their fully charged (+4) oxidation state, leading to a plateau region above 4.5 V. When the material is charged over the transition metal redox reaction region (between 4.4 V and 4.8 V), the reversible oxygen redox process dominates in the bulk and compensates the charge changes during de-lithiation. Both the cation and the anion redox activities offer a reversible capacity/energy density around 300 mA h g^{-1}/1000 W h kg^{-1} at room temperature, in the voltage range from 4.8 to 2.0 V.[32] LMNO is one of the derivatives of spinel $LiMn_2O_4$ material, extensively studied for its high operating voltage (~4.7 V *vs.* Li), high power capability, and good rate capability. Compared with its parent material, this material goes through the majority of electrochemical reaction at a higher voltage due to the redox potential of $Ni^{2+/3+}$ and $Ni^{3+/4+}$ couples. In addition, it has a higher theoretical capacity of 147 mA h g^{-1} and a higher energy density of 650 W h kg^{-1} in the voltage range of 3.5 V to 4.85 V.

2. Experimental

Two types of high-voltage cathode active materials were prepared: $Li(Li_{0.167}Mn_{0.5}Ni_{0.167}Co_{0.167})O_2$ and $Li(Li_{0.144}Mn_{0.544}Ni_{0.136}Co_{0.136})O_2$. The former was obtained from NEI Corporation (Lot #: LMNC-49301) and the latter was synthesized by us, the details of which have been described by Qiu *et al.*[32] $LiMn_{1.5}Ni_{0.5}O_4$ (LMNO) was used for cycling performance testing and the detail of its synthesis and preparation were given by Yoon *et al.*[33]

Active material powders were first blended with polyvinylidene fluoride (PVDF) (Sigma-Aldrich, Product No. 82702) and carbon black (Timcal, C-Nergy Super-C65) with a mass ratio of 80 : 10 : 10. One part of mixed powders were dissolved in one part of 1-methyl-2-pyrrolidone (NMP) to form a slurry, homogenized by using a sonicator (Qsonica, Model no. Q55). The slurry was coated on the current collector by an MTI EQ-Se-KTQ-100 Slurry Coater with the thickness of 300 μm, followed by drying in vacuum for 24 h. The dried electrodes were densified by a steel double-roller (Durston DRM-F150-RE), cut into 14.3 mm-diameter circular pieces, and assembled with membrane separator (Celgard 2320) and lithium metal anode disc (Xiamen TOB, 15.4 mm diameter, 1.1 mm thick) in a MBraun glove box (Argon filled, H_2O < 0.5 ppm). About 30 μL electrolyte (BASF, 1 M $LiPF_6$ in 1 : 1 EC-EMC) was added into the electrode stack before it was sealed into a CR2016 case by an MTI MSK-110 crimper. Two groups of cells, reference and modified cells, were assembled by using electrodes based on flat current collector and functional current collector (FCC), respectively, discussed below. Additional reference cells were produced by using $LiNi_{0.5}Mn_{1.5}O_4$ as the cathode active material;[33] the procedure was similar.

The flat current collector was a regular aluminum foil, 18 μm thick. FCC was produced through debossing the flat current collector with a steel mold. The steel mold was fabricated *via* photolithography (Fig. 1a). First, a 1.6 mm-thick 63.5 mm-wide steel plate (McMaster, 9517K314) was subsequently polished with 200-, 400-, 1200-, and 2500-grit sandpapers, so that the final surface roughness was less than 1 μm. The polished steel surface was cleaned by an Ultrasonic Bath (VWR 50HT) in isopropyl alcohol. Etching resist (Transene PKP-II) was patterned on the steel surface by an EVG 620 Lithography System, with a custom-designed mask manufactured by Fineline Image. The line width and the radius of circles on the mask were 50 μm and 500 μm, respectively; the pattern was double-edged square shaped, as shown in Fig. 1(b–e). Etching was conducted in a nital solution for 120 min at ambient temperature, with the volumetric ratio of nitric acid (65% aqueous solution) and ethanol of 1 : 6. The depth of the etched ridges at the steel surface was ~42 μm and the width was ~25 μm. Debossing was conducted by calendering a sandwich stack formed by the steel mold, an initially flat current collector, and a 1.6 mm-thick polyurethane foam (McMaster, 86375K132), through a steel double-roller (Durston DRM-F150-RE) with the gap opening of 2.2 mm.

The LIB cell was cycled by a Battery Analyzer (MTI BST8-3) for 3 cycles, between 4.8 V and 3.0 V at the rate of 1 C, specified at 300 mA h g^{-1}. After resting for 1 h, the cell was fully charged to 4.8 V, with the specific energy around ~250 mA h g^{-1}. The fully charged cell was impacted in an Instron Ceast 9350 drop tower, with the hammer mass of 5.8 kg and the impact velocity of 1.1 m s^{-1}. Such an impact condition offered an impact energy around 3.5 J. If the impact energy was lower than 3 J, ISC might not be consistently triggered in all the samples; if the impact energy was higher than 4 J, the entire cell case might be penetrated and the temperature measurement could be unreliable. The hammer was dropped onto a 15 mm-long 4.8 mm-diameter steel rod striker resting on a 4.8 mm-diameter spherical ceramic indenter (McMaster, 9599K12). The indenter was then intruded into the LIB cell, promoting the ISC formation. The cell temperature was measured by a type-K thermocouple (Omega TT-K-40-25 gauge 40) connected to a temperature recorder (Omega OM-CP-TEMP101A); the thermocouple was affixed on the top cell surface; the thermocouple tip was around 4 mm away from the indenter. For comparison, impact tests were also performed on fully discharged reference cells.

Cycling tests were carried out at ambient temperature on both $Li(Li_{0.167}Mn_{0.5}Ni_{0.167}Co_{0.167})O_2$ and $LiNi_{0.5}Mn_{1.5}O_4$ cells based on either flat or functional current collectors, by an Arbin Battery Analyzer. The voltage range was 3.0 to 4.85 V for

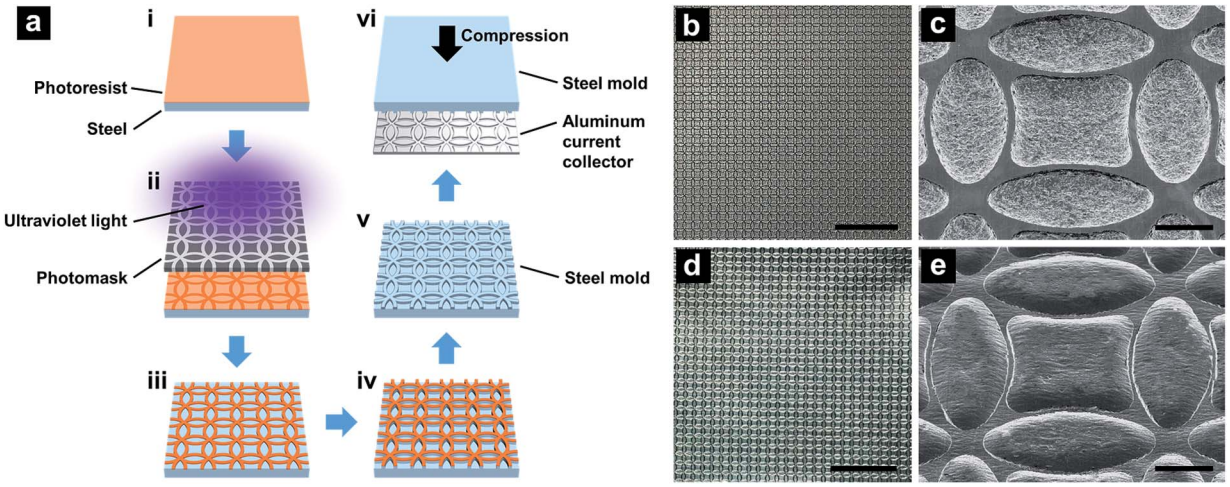

Fig. 1 (a) Processing of functional current collector (FCC): (i) spin coating photoresist on steel plate; (ii) exposure of coated photoresist to ultraviolet light; (iii) photoresist development; (iv) etching of steel plate; (v) photoresist stripping; (vi) debossing and FCC formation. (b) Photo of a steel mold (scale bar: 5 mm). (c) Scanning electron microscope (SEM) image of a steel mold (scale bar: 200 μm). (d) Photo of an FCC (scale bar: 5 mm). (e) SEM image of an FCC (scale bar: 200 μm).

$Li(Li_{0.167}Mn_{0.5}Ni_{0.167}Co_{0.167})O_2$ and 3.5 to 4.85 V for $LiNi_{0.5}Mn_{1.5}O_4$; the cycling rate was C/3.

3. Results and discussion

After a fully charged reference cell is impacted, the cell temperature rapidly increases by ~2.5 °C in 10–20 s (Fig. 2); the maximum temperature increase (ΔT_{max}) of modified cell based on FCC is only ~1 °C, much lower than that of reference cell. More importantly, ΔT_{max} of fully charged modified cell and fully discharge reference cell are similar to each other. In a fully discharged reference cell, there is no stored electric energy; ΔT_{max} is caused by plastic deformation of cell parts that dissipates the impact energy of hammer. Because the cell structure and the impact energy are maintained similar to all the cells, it is clear that ISC-induced heat generation, *i.e.* the release of electrical energy, is negligible in modified cell. The efficiency of FCC for ΔT_{max} reduction is on the same scale for $Li(Li_{0.167}Mn_{0.5}Ni_{0.167}Co_{0.167})O_2$ and $Li(Li_{0.144}Mn_{0.544}Ni_{0.136}Co_{0.136})O_2$.

In general, the heat generation rate (q) of ISC can be assessed as $q = \varepsilon^2/(R + r)$,[34] where ε is the electric potential between cathode and anode, R is the electric resistance of the battery cell, and r is the shorting resistance. In the current study, r is around 0.8 Ω,[31] quite small compared with R. The value of R can be estimated through the voltage drop (ΔU): $R = \Delta U/I$, with I being current. The R values of $Li(Li_{0.167}Mn_{0.5}Ni_{0.167}Co_{0.167})O_2$ and $Li(Li_{0.144}Mn_{0.544}Ni_{0.136}Co_{0.136})O_2$ based cells were measured to be 555 Ω and 571 Ω, respectively. As R is much larger than r and the R values are similar for both active materials, their heat generation rates are also close to each other.

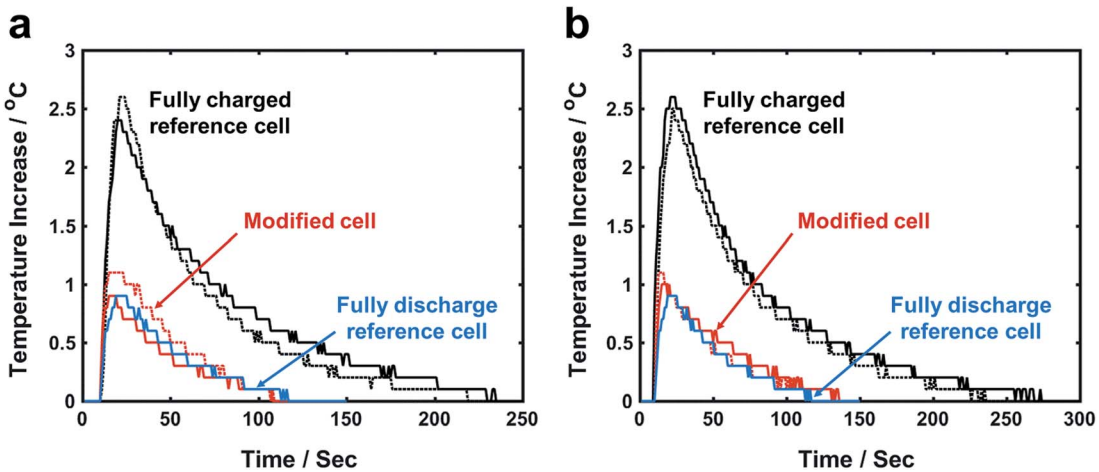

Fig. 2 Temperature profiles of impact tests on (a) $Li(Li_{0.167}Mn_{0.5}Ni_{0.167}Co_{0.167})O_2$ cells and (b) $Li(Li_{0.144}Mn_{0.544}Ni_{0.136}Co_{0.136})O_2$ cells. Solid line and dash line represent different test sample.

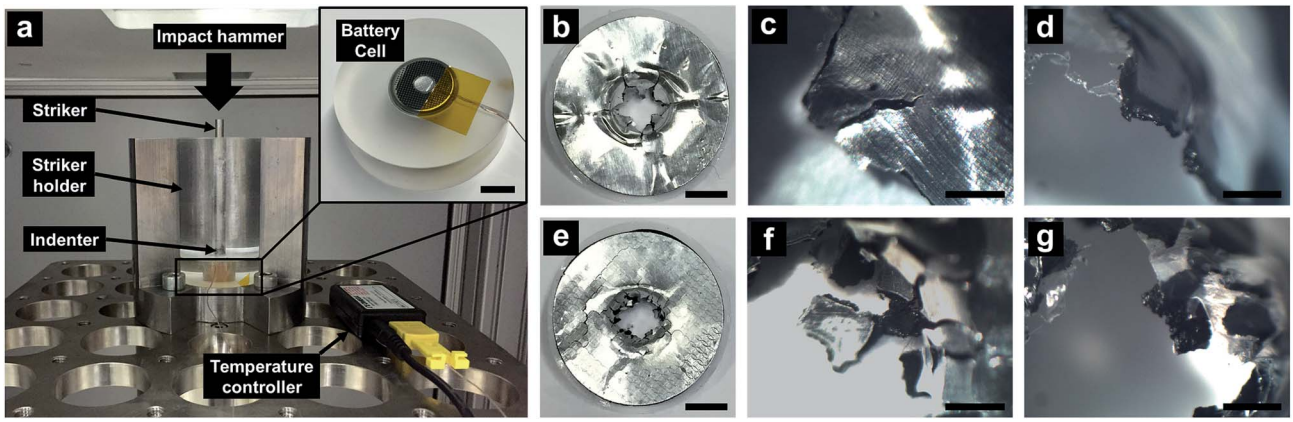

Fig. 3 (a) The impact testing setup (scale bar in the inset: 10 mm). (b) A typical reference electrode after impact test (scale bar: 3 mm). (c) Top view and (d) bottom view of the reference electrode after impact test (scale bar: 500 μm). (e) A typical modified electrode after impact test (scale bar: 3 mm). (f) Top view and (g) bottom view of the modified electrode after impact test (scale bar: 500 μm).

Note that a higher voltage (ε) would cause a faster heat generation rate. Capacitive energy dissipation is dominant in the first few seconds of ISC formation.[35] Most of the stored electrical energy would be dissipated, until the lithium-ions deplete and a new equilibrium is reached. If, instantaneously after the cathode and the anode are shorted, the shorting resistance (r) is drastically raised to much larger than R, ISC-induced heat generation may be decreased.

In an ISC, current passes from the composite cathode layer to the current collector. The collected current flows to the anode side through the shorting spot, where the shorting resistance highly depends on the configuration of the contact between

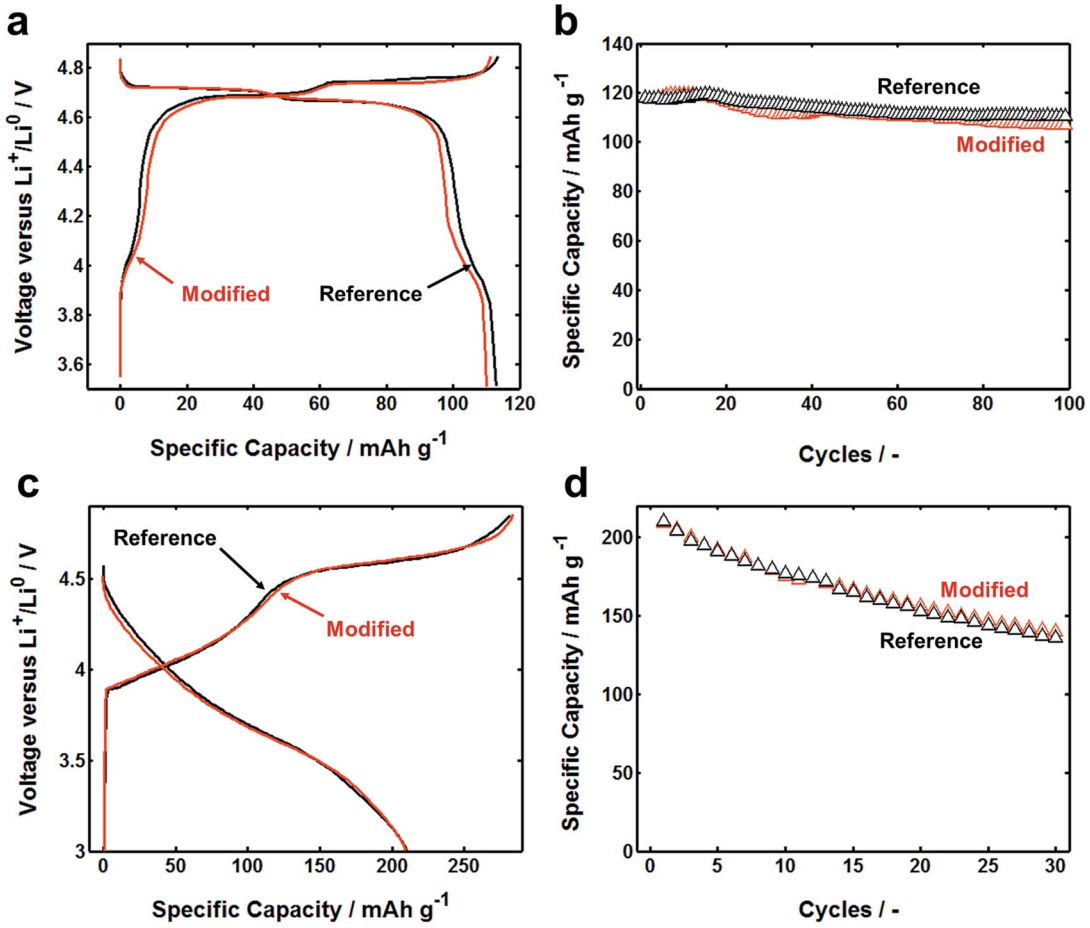

Fig. 4 (a) Typical first-cycle voltage profiles and (b) typical cycling performance of reference and modified cells with LNMO. (c) Typical first-cycle voltage profiles and (d) typical cycling performance of reference and modified cells with LRLO.

cathode and anode. The strength of aluminum current collector is 165 MPa, and the strength of composite electrode layer is only 1–2 MPa.[36] Therefore, the fracture mode of the electrode is dominated by the current collector. On a flat current collector, maximum tensile stresses are along the circular direction, causing nucleation and fast propagation of radial cracks (Fig. 3b–d). As the radial cracks cut through the entire electrode, the petals between them would be bent toward the counter-electrode and become the major conductive paths of ISC. On an FCC, debossing creates a network of surface grooves. They act as stress concentration sites and fundamentally change the stress distribution. At the roots of surface grooves, cracks are initiated after the failure strain is reached; the failure strain of aluminum is around 2%.[30] The cracks tend to propagate along the surface grooves (Fig. 3e–g); particularly, they bifurcate along the double-edged paths, so that the petals among radial cracks are disintegrated by the transverse cracks. The fracture process of the composite electrode layer and the membrane separator follows the same pattern. Consequently, the ISC is completely separated into two parts: the inner area where a small amount of electric energy is released, and the outer area where the electrode behaviors are relatively unrelated to the ISC. As a result, the effective shorting resistance (r) is increased by more than one order of magnitude.[31] Even with the high voltage and the high specific energy of the LIB cells under investigation, because the inner area is only ~10% of the total cell size, the heat generation of ISC is nearly undetectable.

Cycling performance of LIB cells based on flat current collector and FCC is quite similar. LMNO has spinel structure, which has three-dimensional diffusion pathways for lithium-ions. In this structure, metal cations occupy the octahedral sites, similar to layer structured materials, but 1/4 of the metal cations are located in the lithium layers. This leaves 1/4 of transitional metal layer vacant. As a result, Li-ions, occupying in tetrahedral sites of Li layers, share faces with the empty octahedral site. $LiNi_{0.5}Mn_{1.5}O_4$ is known to have a voltage plateau around 4.7 V (ref. 37) (*vs.* Li/Li^+) related to the redox couple of $Ni^{2+/4+}$ and 4.0 V (*vs.* Li/Li^+) plateau was for the redox couple of $Mn^{3+/4+}$. Fig. 4a illustrates typical first-cycle electrochemical charge and discharge voltage profiles between 3.5 and 4.85 V (*vs.* Li/Li^+) with applied constant current of C/3 rates. After 100 cycles, both reference and modified cells have the same capacity retention (Fig. 4b). Similar results were obtained by using LRLO electrode: cells based on reference and modified current collector have similar first cycle charge–discharge curve and similar fading after 30 cycles (Fig. 4c and d). Clearly, the physical configuration of current collector does not much influence the electrochemical reactions. We observed that the bonding between the composite electrode layer and FCC was usually stronger than that of flat current collector, which should be attributed to the increase in contact area.

4. Conclusions

To conclude, we experimentally investigated the effectiveness of functional current collector (FCC) as a cell-level method to reduce heat generation rate in mechanically damaged high-voltage lithium-ion batteries. FCC was produced by debossing flat current collector to form a double-edged square-shaped network of surface grooves. FCC had an entirely different fracture mode from flat current collector, which isolates the internal shorting circuit from the major portion of electrode. It significantly increased the shorting resistance, leading to a much-reduced heat generation rate. The behaviors of FCC were insensitive to the type of active materials under investigation, and did not affect the electrochemical performance under normal working condition. This finding suggests that FCC may be compatible with high-voltage lithium-ion battery chemistry, having important relevance to the future development of safe and robust high-energy large-scale energy storage systems.

Conflicts of interest

There are no conflicts to declare.

Acknowledgements

This research was supported by the Advanced Research Projects Agency-Energy (ARPA-E) under Grant No. DE-AR0000396, for which we are grateful to Dr Ping Liu, Dr John Lemmon, Dr Grigorii Soloveichik, Dr Chris Atkinson, and Dr Dawson Cagle. This work was performed in part at the San Diego Nanotechnology Infrastructure (SDNI) of UCSD, a member of the National Nanotechnology Coordinated Infrastructure, which is supported by the National Science Foundation (Grant ECCS-1542148).

References

1 M. Armand and J.-M. Tarascon, *Nature*, 2008, **451**, 652–657.
2 H. Ibrahim, A. Ilinca and J. Perron, *Renewable Sustainable Energy Rev.*, 2008, **12**, 1221–1250.
3 H. Chen, T. N. Cong, W. Yang, C. Tan, Y. Li and Y. Ding, *Prog. Nat. Sci.*, 2009, **19**, 291–312.
4 A. Manthiram, Y. Fu and Y.-S. Su, *Acc. Chem. Res.*, 2012, **46**, 1125–1134.
5 C. R. Wilkinson and J. G. Anderson, *An introduction to detonation and blast for the non-specialist*, 2003.
6 N. Williard, W. He, C. Hendricks and M. Pecht, *Energies*, 2013, **6**, 4682–4695.
7 M. Jacoby, *Chem. Eng. News*, 2013, **91**, 33–37.
8 https://electrek.co/2016/08/15/tesla-model-s-catches-fire-test-drive-france, accessed June 2016.
9 https://electrek.co/2017/03/31/tesla-model-s-fire-manchester-crash, accessed June 2016.
10 A. Saini and M. Austin, *MRS Bull.*, 2017, **42**, 414–415.
11 S. Whittingham, *MRS Bull.*, 2017, **42**, 413.
12 L. Lu, X. Han, J. Li, J. Hua and M. Ouyang, *J. Power Sources*, 2013, **226**, 272–288.
13 Z. Qian, Y. Li and Z. Rao, *Energy Convers. Manage.*, 2016, **126**, 622–631.
14 A. Augeard, T. Singo, P. Desprez, F. Perisse, S. Menecier and M. h. Abbaoui, *2014 IEEE 60th Holm Conference*, 2014.

15 E. Sahraei, J. Campbell and T. Wierzbicki, *J. Power Sources*, 2012, **220**, 360–372.
16 A. Hammami, N. Raymond and M. Armand, *Nature*, 2003, **424**, 635–636.
17 X. Feng, M. Fang, X. He, M. Ouyang, L. Lu, H. Wang and M. Zhang, *J. Power Sources*, 2014, **255**, 294–301.
18 Q. Wang, P. Ping, X. Zhao, G. Chu, J. Sun and C. Chen, *J. Power Sources*, 2012, **208**, 210–224.
19 A. Hofmann, N. Uhlmann, C. Ziebert, O. Wiegand, A. Schmidt and T. Hanemann, *Appl. Therm. Eng.*, 2017, **124**, 539–544.
20 G. Venugopal, *J. Power Sources*, 2001, **101**, 231–237.
21 E. Roth, D. Doughty and D. Pile, *J. Power Sources*, 2007, **174**, 579–583.
22 M. Baginska, B. J. Blaiszik, R. J. Merriman, N. R. Sottos, J. S. Moore and S. R. White, *Adv. Energy Mater.*, 2012, **2**, 583–590.
23 Z. Chen, P.-C. Hsu, J. Lopez, Y. Li, J. W. To, N. Liu, C. Wang, S. C. Andrews, J. Liu and Y. Cui, *Nat. Energy*, 2016, **1**, 15009.
24 H. Zhang, J. Pang, X. Ai, Y. Cao, H. Yang and S. Lu, *Electrochim. Acta*, 2016, **187**, 173–178.
25 P. Balakrishnan, R. Ramesh and T. P. Kumar, *J. Power Sources*, 2006, **155**, 401–414.
26 A. V. Le, M. Wang, Y. Shi, D. Noelle, Y. Qiao and W. Lu, *J. Appl. Phys.*, 2015, **118**, 085312.
27 A. V. Le, M. Wang, Y. Shi, D. J. Noelle and Y. Qiao, *J. Phys. D Appl. Phys.*, 2015, **48**, 385501.
28 M. Wang, A. V. Le, Y. Shi, D. J. Noelle, H. Yoon, M. Zhang, Y. S. Meng and Y. Qiao, *J. Mater. Sci. Technol.*, 2016, **32**, 1117–1121.
29 M. Wang, A. V. Le, D. J. Noelle, Y. Shi, H. Yoon, M. Zhang, Y. S. Meng and Y. Qiao, *Int. J. Damage Mech.*, 2016, 1056789516660176.
30 M. Wang, A. V. Le, Y. Shi, D. J. Noelle and Y. Qiao, *Appl. Phys. Lett.*, 2017, **110**, 083902.
31 M. Wang, A. V. Le, D. J. Noelle, Y. Shi, Y. S. Meng and Y. Qiao, *J. Power Sources*, 2017, **349**, 84–93.
32 B. Qiu, M. Zhang, L. Wu, J. Wang, Y. Xia, D. Qian, H. Liu, S. Hy, Y. Chen, K. An, Y. Zhu, Z. Liu and Y. S. Meng, *Nat. Commun.*, 2016, **7**, 12108.
33 H. Yoon, PhD thesis, University of California, San Diego, 2016.
34 W. Fang, P. Ramadass and Z. J. Zhang, *J. Power Sources*, 2014, **248**, 1090–1098.
35 T. G. Zavalis, M. Behm and G. Lindbergh, *J. Electrochem. Soc.*, 2012, **159**, A848–A859.
36 P. Liu, E. Sherman and A. Jacobsen, *J. Power Sources*, 2009, **189**, 646–650.
37 G. Cheng, P. Zuo, L. Wang, W. Shi, Y. Ma, C. Du, X. Cheng, Y. Gao and G. Yin, *J. Solid State Electrochem.*, 2015, **19**, 281–288.